

Hard X-ray flares and spectral variability in NGC 4395 ULX1

TANUMAN GHOSH,¹ VIKRAM RANA,¹ AND MATTEO BACHETTI²

¹*Department of Astronomy & Astrophysics, Raman Research Institute, C. V. Raman Avenue, Sadashivanagar, Bangalore 560080, India*

²*Istituto Nazionale di Astrofisica-Osservatorio Astronomico di Cagliari, via della Scienza 5, I-09047 Selargius (CA), Italy*

ABSTRACT

We report the detection of flaring events in NGC 4395 ULX1, a nearby ultraluminous X-ray source(ULX), for the first time, using recent *XMM-NEWTON* observations. The flaring episodes are spectrally harder than the steady emission periods, resulting in higher fractional variability in the high energy regime. A thin Keplerian and a slim accretion disk provide the best-fit continuum for *XMM-NEWTON* spectra. In all observations, the presence of a broad Gaussian emission feature around ~ 0.9 keV suggests a strong wind outflow in this ULX. The flaring spectra correspond to higher slim disk temperatures due to higher mass accretion rate under an advection-dominated accretion scenario. The luminosity-temperature profile in different flux states is consistent with the theoretical predictions for a slim accretion disk in the case of super-Eddington accretion onto a stellar-mass compact object. The unperturbed absorption column and wind outflow line emission during flaring events suggest that the site of origin of these flares is mainly the advection flow in the inner region of the accretion disk.

Keywords: Ultraluminous x-ray sources (2164) — X-ray binary stars (1811)

1. INTRODUCTION

Ultraluminous X-ray sources are the brightest off-nuclear X-ray binaries, having emission luminosities above the Eddington limit of a $10 M_{\odot}$ black hole ($L_x > 10^{39}$ erg s⁻¹; see Kaaret et al. (2017) for a recent review). Compared to the sub-Eddington Galactic X-ray binaries(XRBs) or active galactic nuclei(AGNs), ULXs show distinct spectral curvature below 10 keV, suggesting that these sources are mostly super-Eddington stellar-mass compact objects. Indeed a number of ULXs were found to have neutron star accretors, confirming this super-Eddington interpretation (Bachetti et al. 2014; Fürst et al. 2016; Israel et al. 2017a,b; Brightman et al. 2018; Chandra et al. 2020; Carpano et al. 2018; Rodríguez Castillo et al. 2020; Sathyaprakash et al. 2019).

ULX spectra show two common features - a characteristic turnover below 10 keV and a soft excess ≤ 1 keV. These properties are typically explained by disk wind emission in the scenario of super-Eddington accretion (Shakura & Sunyaev 1973; Poutanen et al. 2007). The

mass outflow rate and the viewing angle of the disk determine the spectral softness, with softer sources being observed closer to the disk plane (see Pinto et al. (2021) and references therein). Strong blue-shifted atomic features are one of the signature characteristics of such relativistic ($\beta \sim 0.25$) wind emission (Pinto et al. 2016, 2017; Kosec et al. 2018a,b; Walton et al. 2016; Middleton et al. 2015; Pinto et al. 2020) which can share a large fraction of the total energetic budget of ULXs.

Modern X-ray instruments have observed a large number of ULXs. However, few sources have shown short-term timing variability in terms of fractional variability, quasi-periodic or periodic oscillation. A number of sources like NGC 1313 X1 (Walton et al. 2020), NGC 7456 ULX-1 (Pintore et al. 2020), NGC 253 ULX-1 (Barnard 2010), NGC 6946 ULX-3 (Earnshaw et al. 2019), NGC 247 ULX-1 (Pinto et al. 2021), 4XMM J111816.0-324910 in NGC 3621 (Motta et al. 2020), NGC 4559 X7 (Pintore et al. 2021), M82 X-1 (Brightman et al. 2016) have been found showing some intermittent flaring events. These flaring activities can help shed light on the accretion state transitions in these sources.

NGC 4395 ULX1 (2XMM J122601.4+333131; Liu & Bregman (2005)) is a ULX which has shown a long term variability (Kaaret & Feng 2009) and exhibited a period

of 62.8 days (Vinokurov et al. 2018) in archival observations. A previous study (Earnshaw & Roberts 2017) showed no significant short-term timing variability in this source. In this paper, we present a detailed study of four high-quality *XMM-NEWTON* observations, two of which show flaring activities from this source for the first time.

2. DATA ANALYSIS

XMM-NEWTON observed the NGC 4395 galaxy four times between December 2018 and January 2019, to study the AGN (Pi McHardy). ULX1 is around ~ 3 arcmin away from the galaxy’s active nucleus. In the *XMM-NEWTON* EPIC detectors, ULX1 is well isolated from any other X-ray sources. The details of the observation log are given in table 1.

Using the standard data reduction procedure of *XMM-NEWTON* data analysis software SAS v19.1.0¹, we clean the data from soft-proton and background flaring events, and extract the science products for all EPIC-pn and MOS1/2 instruments. We select source counts from a circle of 25 arcsec radius centered at $\alpha, \delta = 12 : 26 : 01.5, +33 : 31 : 31.0$ and background counts from a circle of 50 arcsec radius in a nearby source-free region on the same chip.

Unfortunately, ULX1 falls near the chip gap in all pn data. Additionally, the pn data are affected by bad column events in the source region in all observations. XM3 and XM4 data are mostly affected because the bad column falls through the centroid of the source. This causes a significant flux loss in pn spectra due to substantial charge loss. XM1 and XM2 pn data are comparatively less affected because the bad column falls through the edge of the source.

The fast timing analysis is done on minimally-filtered data, in order to maximize the number of counts and be sensitive to short-time variability. However, for the spectral analysis, we put a strict constrain of FLAG==0 to extract pn spectra for all observations to minimize the charge loss effect in the data. Spectra are grouped to have a minimum of 20 counts per energy bin for using χ^2 statistics. Light curves are extracted using EVSELECT for single and double events in pn (PATTERN ≤ 4) and singles, doubles, triples, and quadruples events in MOS (PATTERN ≤ 12). The background-corrected source light curves are generated using the EPICLC-CORR task, which corrects vignetting, bad pixels, chip

gaps, PSF, and quantum efficiency. Pileup in the data is evaluated with EPATPLOT, and no significant pileup is found.

3. TIMING ANALYSIS

Previous X-ray observations portrayed NGC 4395 ULX1 as the least variable source in a sample of soft ULXs studied in Earnshaw & Roberts (2017). However, the *XMM-NEWTON* observations analyzed here show both short-term (in the time scale of a few kilo seconds) and long-term (in the time scale of a few days) timing variability.

The 2000-s binned *XMM-NEWTON* pn lightcurves for all epochs are shown in figure 1. From a visual inspection, it appears that while in XM1 and XM3 the source has a relatively steady flux, in XM2 and XM4 it shows flare-like activity. In order to check any energy dependent nature of flaring behavior, we divide the time series into two energy bands. We set the soft band between 0.3 and 1 keV (figure 1-first panel), and the hard band is above 1 keV (second panel). We set the upper limit for the hard band to the energy at which background dominates (see Section 4.1), which is 5 keV for XM1 and XM3, and 8 keV for XM2 and XM4. The hardness ratio in figure 1-third panel, is defined as the ratio of hard photon count rate to soft photon count rate. The fourth panel of the figure shows the sum of soft and hard band lightcurves. The figure shows how the ULX1 count rate varies between different epochs around three weeks of time scale. The XM2 observation shows a significant short-term flaring incident lasting ~ 50 ksec mostly prominent in hard energy band. The longest flaring episode is detected during the XM4 observation, where the flaring happened for ~ 80 ksec, a large portion of the observing span. The long flare of XM4 epoch consists of multiple ephemeral sub-flaring episodes. However, the minimum count rate level of these transient sub-flares is much higher than the persistent count rate level of the XM1 and XM3 epochs. So, we consider the whole ~ 80 ksec long flare in XM4 as a single flaring epoch for our analysis. As there are no flaring events in XM1 and XM3, the hardness ratio is nearly constant for these two epochs. On the other hand, for XM2 and XM4, the hardness ratio demonstrates that the variability in different energy bands is prominent, and the flaring events are more significant in the harder spectral band (above ~ 1 keV).

Studying short-term variability is essential to decipher the inherent properties of transient events happening in ULXs. The first task to find such variability is to perform a Fourier space investigation of the time series. The power spectral density (PSD) analysis pro-

¹ <https://www.cosmos.esa.int/web/xmm-newton/sas>

Table 1. Observation log of NGC 4395 ULX1

Serial No.	Observation ID	Date of Obs.	Epoch ID	Cleaned Exposure (ksec)
				pn/MOS1/MOS2
1	824610101	2018-12-13	XM1	71/89/94
2	824610201	2018-12-19	XM2	47/67/69
3	824610301	2018-12-31	XM3	50/66/70
4	824610401	2019-01-02	XM4	77/97/100

NOTE—The exposure times noted here are flare corrected livetime CCD exposures.

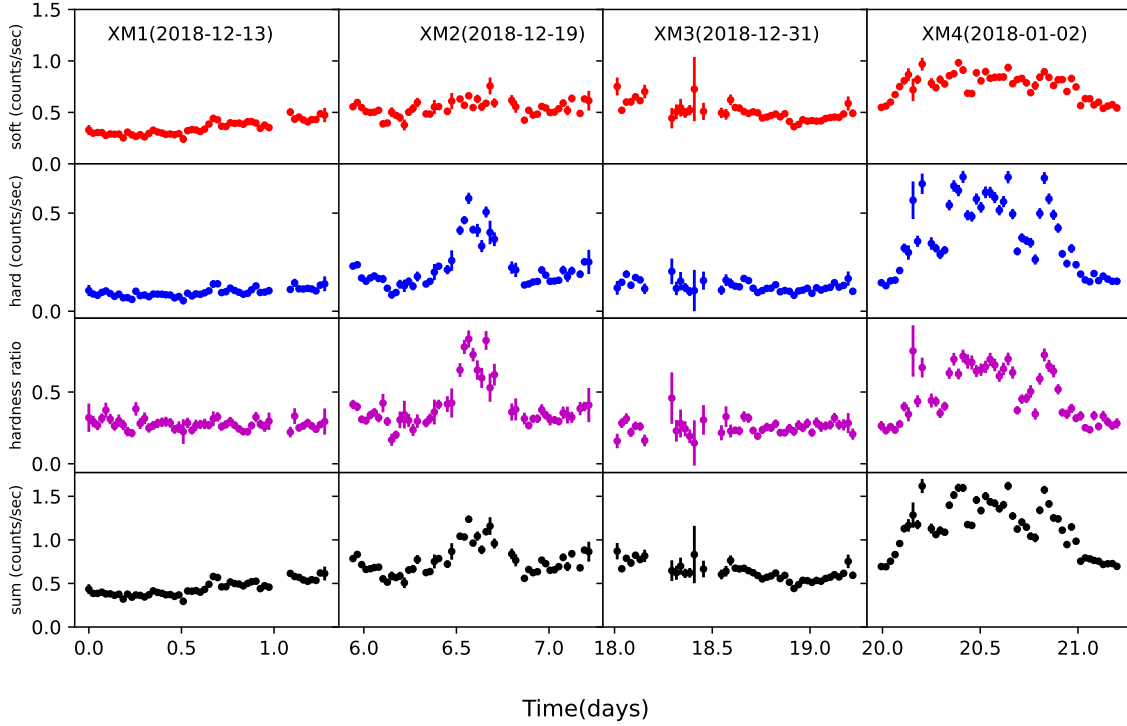


Figure 1. *XMM-NEWTON* pn light curves of ULX1 for four individual epochs binned by 2000 seconds. The first panel shows the soft (0.3 – 1.0 keV) count rate; the second panel shows the hard (1.0 – 5.0 keV for XM1 and XM3 and 1.0 – 8.0 keV for XM2 and XM4) count rate, the third panel shows the hardness ratio defined as hard/soft photons count rate and the fourth panel shows the sum of soft and hard band lightcurve, i.e. the total lightcurve. First epoch (XM1) - shows a steady but slight uprising trend of the flux, Second Epoch (XM2) - A flaring episode occurred from around 30 ksec to 80 ksec of that observation, Third Epoch (XM3) - shows another steady but slightly declining trend of flux, Fourth Epoch (XM4) - finally, a large flaring episode happened covering most portion (~ 80 ksec) of that observation. The prominent flares in XM2 and XM4 are predominant in the hard band, as seen in the hardness ratio plots.

vides no evidence of quasi-periodic or periodic oscillation in any of the observations except the presence of red noise at low frequencies in a few cases. We also search for transient pulsation in the time series. We incorporate the acceleration search technique to detect any transient pulse while correcting the Doppler shift due to binary orbital period correction. Tools like HENDRICS (Bachetti 2018) and PRESTO (Ransom 2011) are employed for these tasks. However, no significant pulsation is detected in any epoch. We further divide XM2 and XM4 observations into three sub-epochs (see figure 2 left and right panel respectively): pre-flare, flare and post-flare epochs. Pre-flare and post-flare epochs have similar count rates and overlapping spectral properties. Hence they are combined as “non-flaring” epochs. We also perform a similar exercise to search pulsation in those segmented “flaring” and “non-flaring” lightcurves using the aforementioned methods. No pulse period is found in either case.

These lightcurves also demonstrate significant short-term variability in terms of the fractional root mean square (RMS) variability amplitude (F_{var}), which measures the variance of a source over the Poissonian noise in the time series, normalized to the average count rate (Vaughan et al. 2003; Edelson et al. 2002). $F_{var} = \sqrt{\frac{S^2 - \bar{\sigma}^2}{\bar{x}^2}}$, where $S^2 = \frac{1}{N-1} \sum_{i=1}^N (x_i - \bar{x})^2$ and $\bar{\sigma}^2 = \frac{1}{N} \sum_{i=1}^N \sigma_i^2$. x_i is the count rate at i ’th bin, \bar{x} is the mean count rate, N is the total number of bins, σ_i is the uncertainty in count rate in i ’th bin. The error on F_{var} is measured as $\sigma_{F_{var}} = \frac{1}{F_{var}} \sqrt{\frac{1}{2N} \frac{S^2}{\bar{x}^2}}$. We use the soft and hard lightcurves of each *XMM-NEWTON* pn observation and bin them to 1000 sec, then we estimate the F_{var} and its error. For XM1, these values are 0.17 ± 0.02 for both soft and hard energy lightcurves. Similarly for XM3, these values are 0.18 ± 0.02 and 0.14 ± 0.04 respectively. However, for XM2, the values are 0.11 ± 0.01 and 0.52 ± 0.04 , and for XM4, they are 0.15 ± 0.01 and 0.47 ± 0.03 in the soft band and hard band respectively. To verify, that these differences in variability are not coming from the bad column in pn, described in section 2, we perform a similar exercise with the MOS data that are free of any such bad column issue. First we add MOS1 and MOS2 light curves to increase the count statistics (for both soft and hard energy band) and rebin the net light curves by 1000 sec. We find that for XM1 epoch, the soft and hard band fractional variability values are 0.16 ± 0.02 , 0.12 ± 0.04 respectively. Similarly for XM3, these values are 0.21 ± 0.02 and 0.13 ± 0.03 respectively. However, for XM2 these are 0.12 ± 0.02 and 0.47 ± 0.04 respectively, and for XM4, the soft band and hard band fractional variabilities are 0.17 ± 0.1 and

0.47 ± 0.03 respectively. Hence, we can confirm that these variabilities are intrinsic property of ULX1 and not arising due to bad column issue. This shows that fractional variability is higher in epochs XM2 and XM4 compared to the epochs XM1 and XM3 above 1.0 keV energy band. Nonetheless, the variability below 1.0 keV is lower and relatively steady between all epochs.

4. SPECTRAL ANALYSIS

In this section, we report the spectral analysis results of the *XMM-NEWTON* observations in detail. We use XSPECv12.12.0 for the spectral analysis throughout the paper. The absorption is quantified using the Tuebingen-Boulder ISM absorption model (TBABS in XSPEC) for Galactic and local extinction contributions. The updated abundance (Wilms et al. 2000) and photoionization cross-section (Verner et al. 1996) are used. The Galactic absorption column² is kept fixed to $0.04 \times 10^{22} \text{ cm}^{-2}$. The local absorption column is allowed to vary as a free parameter.

4.1. Time averaged spectroscopy

We start by analyzing the spectra of individual observations. We plot MOS1 spectra for all epochs (top left panel) in figure 3. XM1 and XM3 have similar spectra in terms of flux and spectral feature, and both of them exhibit steep spectra extending only up to 5 keV, after which background starts dominating. XM2 and XM4 epochs have comparatively harder spectra and higher flux than the other two epochs and extend up to 8 keV, after which the signal-to-noise ratio decreases significantly.

Since there is a bad column issue in pn data, we perform an exercise to verify whether the bad column affects the source spectral properties. First of all, we carry out an individual analysis of pn and MOS1/2 data for all observations with a simple absorbed powerlaw model and a Gaussian component (see details of spectral models below) and find that the spectral parameters in the pn data are consistent with MOS1/2 data within 90% statistical confidence interval, with the only exception of the normalization of the power law in XM3 and XM4. Therefore, in the following, we simultaneously fit pn and MOS1/2 data for each observation with a cross-calibration constant fixed to 1 for MOS1, and left free to vary in MOS2 and pn. All other parameters of the models used are tied between the instruments. These cross-calibration values are within 10% of MOS1, except for pn data of XM3 and XM4 epochs, the ones

² <https://heasarc.gsfc.nasa.gov/cgi-bin/Tools/w3nh/w3nh.pl>

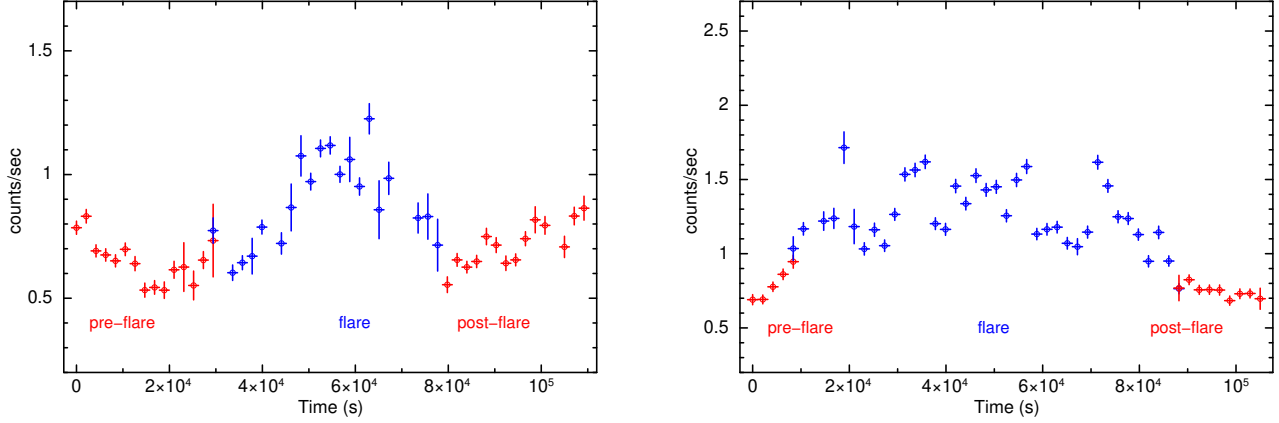


Figure 2. Different transient episodes are defined for XM2 (left) and XM4 (right) epochs of observation. The pre-flare, flare, and post-flare epochs are separately indicated. The pre-flare and post-flare epochs are combined to get the “non-flaring” state.

most affected by the noisy detector column described in Section 2.

To quantify the contribution of different emission mechanisms in ULX1 spectra, we fit them with various physical and phenomenological models in XSPEC. A simple power-law fit is useful to characterize the spectral hardness of the individual epochs. XM1 and XM3 epochs have power-law index (Γ) value of ~ 4.6 and ~ 4.8 respectively, whereas XM2 and XM4 epochs have ~ 3.7 and ~ 3.5 respectively. Using this powerlaw continuum, a soft excess around ~ 0.4 keV and a Gaussian emission-like feature around ~ 0.9 keV are also detected. If we use a more complicated model composed of a thermal blackbody disk, a power-law, and a Gaussian, we are able to fit the ULX1 spectra at all epochs. However, the parameters of the power-law model are degenerate with those of the low energy components like the extinction or the emission lines. Hence, we explore other models, seeking a physically-consistent description of ULX1 spectra.

Many ULX spectra, from soft ULXs like NGC 55 ULX and NGC 247 ULX-1 to moderately hard ULXs like NGC 1313 X1 and NGC 4559 X7, have been modeled with the composition of two thermal component models (Pinto et al. 2017, 2020; Kara et al. 2020; Walton et al. 2020; Pintore et al. 2021). For NGC 4395 ULX1, we find that one cool thin disk (DISKBB in XSPEC) plus a comparatively hotter slim accretion disk (DISKPBB in XSPEC, with $p = 0.50$) provide an adequate fit for the continuum at all epochs. A broad Gaussian around 0.9 keV is always required. In XSPEC syntax, the best fit model we use is `TBABS(GAL)*TBABS*(GAUSS+DISKBB+DISKPBB)`. We find that the temperature dependence parameter “p” of

DISKPBB always assumes a value close to lower limit of the parameter, 0.50, corresponding to a slim disk regime. Hence we fix this “p” value to 0.50. The nH value is consistent in all epochs ($\sim 0.05 \times 10^{22} \text{ cm}^{-2}$), and so is the Gaussian line energy (~ 0.9 keV). The low-energy thin disk component (represented by the DISKBB model) also remains in a similar temperature state in all epochs. However, the DISKPBB component exhibits a higher temperature in the epochs XM2 and XM4 compared to the epochs XM1 and XM3. The average DISKPBB temperature in XM2 and XM4 epochs is ~ 1.5 times higher than that in XM1 and XM3 epochs. The best-fit parameters are noted in table 2 and the residuals for MOS1 spectra are shown in bottom left panel of figure 3 for each observation without the Gaussian component. Presence of prominent hump like (or Gaussian) structure is evident from the residual plots.

4.2. Time-resolved spectroscopy

ULX1 has undergone several flaring episodes, as described in section 3. This motivates us to carry out a comparative study of the source’s spectral properties between flaring and non-flaring epochs. This subsection mainly focuses on epochs XM2 and XM4, where flares are prominent. As described earlier, we divide the XM2 and XM4 epochs into three sub-epochs: pre-flare, flare, and post-flare. Non-flaring events are chosen by adding the pre-flare and post-flare regime events because the spectral flux and properties overlap during these regimes. In figure 3 (top middle (XM2) and right (XM4) panel), we overplot the flaring and non-flaring spectra from MOS1. This figure shows how spectra of

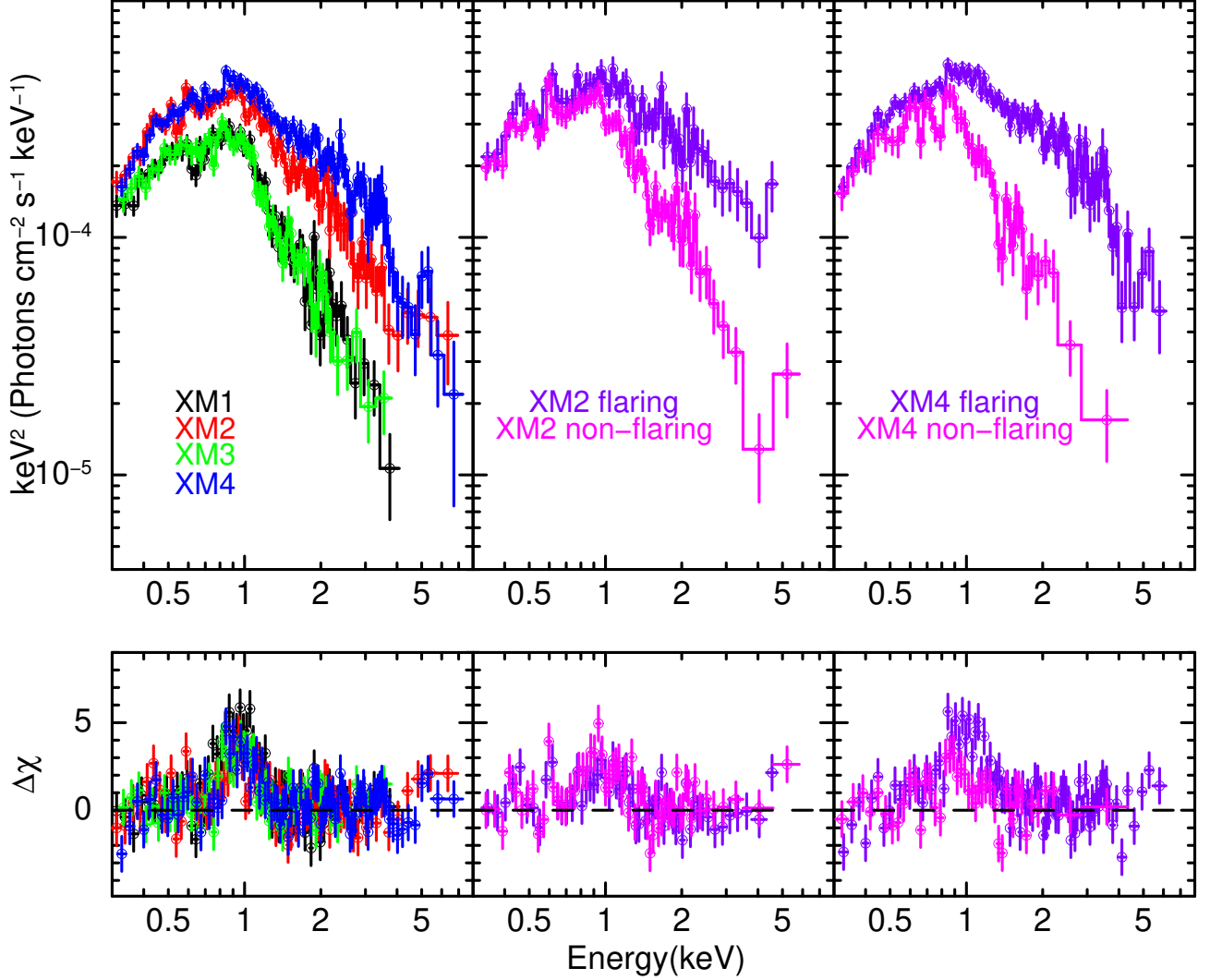


Figure 3. Top: ULX1 exhibiting a significant long-term spectral variability in different observation epochs. MOS1 spectra of XM1 and XM3 epochs in the left panel show overlapping spectral features. XM2 and XM4 epochs clearly show differences in spectral shapes and divergence in hard spectral regimes. Flaring and non-flaring spectra of XM2 and XM4 epochs are plotted in the middle and right panels. These two figures have a similar divergence in spectral characteristics above 1 keV. Bottom: The residuals of the best fit continuum without the Gaussian component are shown for MOS1 spectra corresponding to the epochs shown in the top panels.

flaring and non-flaring states diverge mainly after 1 keV (as in part already shown from the timing analysis). Below 1 keV, the spectra are mostly consistent.

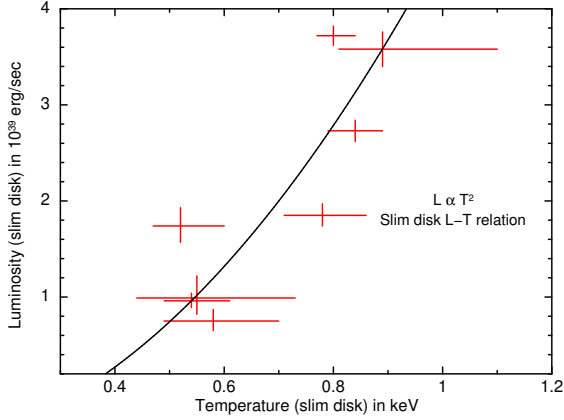
We fit these time-resolved spectra with the same model used for the time-averaged analysis, since it was adequate to describe both the steady (XM1 and XM3) and the non-steady (XM2 and XM4) observations. The

fit of non-flaring and flaring spectra of individual observation is done simultaneously, linking absorption and line energy and letting the disk parameters vary freely. We report the best fit parameter and error estimates in table 3. Figure 3(bottom middle (XM2) and right (XM4) panel) shows the residuals (without the Gaussian component) for MOS1 spectra. The non-varying

Table 2. Best fit model (TBABS(GAL)*TBABS*(GAUSS+DISKBB+DISKPBB)) parameters of NGC 4395 ULX1 for the four epochs.

Parameter	Unit	XM1	XM3	XM2	XM4
nH	10^{22}cm^{-2}	$0.05^{+0.03}_{-0.02}$	$0.06^{+0.03}_{-0.02}$	0.04 ± 0.01	0.05 ± 0.01
$lineE$	keV	0.91 ± 0.02	0.92 ± 0.02	$0.92^{+0.03}_{-0.04}$	$0.95^{+0.02}_{-0.03}$
σ	keV	$0.15^{+0.03}_{-0.02}$	$0.11^{+0.03}_{-0.02}$	$0.14^{+0.04}_{-0.03}$	0.13 ± 0.03
$norm$	10^{-5}	$5.71^{+2.90}_{-1.54}$	$3.68^{+2.03}_{-0.96}$	$4.12^{+2.44}_{-1.33}$	$3.86^{+1.67}_{-1.03}$
T_{thin}	keV	$0.17^{+0.03}_{-0.04}$	$0.18^{+0.02}_{-0.03}$	$0.22^{+0.02}_{-0.03}$	$0.22^{+0.02}_{-0.03}$
$norm_{thin}$		$55.29^{+94.71}_{-28.47}$	$42.13^{+84.76}_{-18.30}$	$19.94^{+18.55}_{-7.09}$	$16.10^{+13.24}_{-5.87}$
T_{slim}	keV	$0.54^{+0.07}_{-0.05}$	$0.58^{+0.12}_{-0.09}$	$0.78^{+0.08}_{-0.07}$	0.84 ± 0.05
$norm_{slim}$		$0.06^{+0.04}_{-0.03}$	$0.03^{+0.06}_{-0.02}$	0.02 ± 0.01	0.02 ± 0.01
χ^2/dof		165/168	150/140	218/206	275/238
F_x	$10^{-13} \text{ergs/cm}^2/\text{s}$	5.31 ± 0.12	$5.26^{+0.13}_{-0.14}$	9.24 ± 0.18	$11.06^{+0.17}_{-0.16}$
L_x	10^{39}ergs/s	1.44 ± 0.03	1.43 ± 0.04	2.51 ± 0.05	$3.0^{+0.05}_{-0.04}$

NOTE—The absorbed flux and luminosity is calculated in 0.3-10.0 keV energy range. The Galactic absorption was fixed to $0.04 \times 10^{22} \text{cm}^{-2}$. “p” value of diskpbb model is fixed to 0.50, resembling a slim disk. The distance is assumed to be 4.76 Mpc (Vinokurov et al. 2018) to calculate the luminosity.

**Figure 4.** Relation between unabsorbed luminosity of the hard slim disk component vs. temperature of that disk. This follows the $L \propto T^2$ curve

nature of DISKBB temperature between flaring and non-flaring epochs are similar to the case of time-averaged spectroscopic results reported in table 2. The best fit DISKPBB temperatures in flaring epochs are higher than that in non-flaring epochs of XM2 and XM4 by a factor of ~ 1.7 and ~ 1.5 times respectively.

5. DISCUSSION AND CONCLUSIONS

A previous study by Earnshaw & Roberts (2017) showed that the spectra from ULX1 exhibit a steep powerlaw tail and a strong, Gaussian-like, feature near ~ 0.9 keV, which could be explained by a mekal model. However, multiple studies suggest that two-component disks might be more appropriate to describe spectra of ULXs (Pinto et al. 2017, 2020; Kara et al. 2020; Walton et al. 2020).

It is widely believed that disks around ULXs have a two-tiered structure: very far from the ULX, the disk is a typical Shakura & Sunyaev (1973)-like thin disk. Once the local luminosity of the disk approaches the Eddington limit, the disk “inflates”, winds are launched carrying away excess mass and advection plays a central role. In this physical scenario, the low-energy thin disk component corresponds to the outer disk, and the high-energy slim disk component corresponds to the emission from the inner disk and the winds. By setting this physical accretion picture, we will discuss how these new XMM-NEWTON observations conform with these scenarios.

The XMM-NEWTON observations of NGC 4395 ULX1 before 2018 do not show significant short-term variability in the source (Earnshaw & Roberts 2017). The latest 2018-2019 observations, however, show significant flaring episodes in the data. We observe that the spectral properties are similar to the moderately luminous ULXs in the “broadened disk” state (Sutton et al. 2013). Although the source has a signifi-

Table 3. Time resolved spectral parameters of XM2 and XM4 epochs using best fit model same as in table 2

Parameter	Unit	XM2		XM4	
		flaring	non-flaring	flaring	non-flaring
nH	10^{22} cm^{-2}	$0.05^{+0.06}_{-0.02}$		0.07 ± 0.02	
$lineE$	keV	$0.90^{+0.03}_{-0.02}$		$0.91^{+0.02}_{-0.04}$	
σ	keV	$0.19^{+0.11}_{-0.08}$	$0.15^{+0.12}_{-0.05}$	$0.21^{+0.02}_{-0.03}$	$0.09^{+0.04}_{-0.03}$
$norm$	10^{-5}	$7.10^{+10.99}_{-4.66}$	$5.83^{+22.47}_{-2.5}$	$9.65^{+4.47}_{-3.45}$	$4.36^{+5.35}_{-1.42}$
T_{thin}	keV	$0.18^{+0.10}_{-0.09}$	$0.18^{+0.04}_{-0.09}$	$0.15^{+0.08}_{-0.02}$	$0.18^{+0.02}_{-0.05}$
$norm_{thin}$		$32.32^{+4390.61}_{-26.85}$	$41.23^{+4685.61}_{-23.10}$	$69.23^{+258.31}_{-59.65}$	$58.15^{+203.35}_{-26.74}$
T_{slim}	keV	$0.89^{+0.21}_{-0.08}$	$0.52^{+0.08}_{-0.05}$	$0.80^{+0.04}_{-0.03}$	$0.55^{+0.18}_{-0.11}$
$norm_{slim}$		0.02 ± 0.01	$0.11^{+0.12}_{-0.07}$	0.04 ± 0.01	$0.05^{+0.14}_{-0.04}$
χ^2/dof		349/327		409/344	
F_x	$10^{-13} \text{ ergs/cm}^2/\text{s}$	12.36 ± 0.40	7.87 ± 0.19	$12.49^{+0.20}_{-0.21}$	6.50 ± 0.24
L_x	10^{39} ergs/s	3.35 ± 0.11	2.14 ± 0.05	3.39 ± 0.06	1.76 ± 0.06

NOTE—The absorbed flux and luminosity is calculated in 0.3-10.0 keV energy range. The Galactic absorption was fixed to $0.04 \times 10^{22} \text{ cm}^{-2}$. “p” value of diskpbb model is fixed to 0.50, resembling a slim disk. The distance is assumed to be 4.76 Mpc (Vinokurov et al. 2018) to calculate the luminosity.

cantly soft spectrum, the luminosity measurement ($L \sim 1.4 - 3.0 \times 10^{39} \text{ ergs s}^{-1}$) shows that ULX1 is accreting just above the Eddington accretion rate limit if it hosts a stellar-mass compact object. So, the source is far from the luminosity range of ULXs in soft ultraluminous state (Sutton et al. 2013) or soft-bright state (Gúrpidé et al. 2021a,b). One possible explanation for the soft nature of the source is a geometrical picture when the inclination angle with the line of sight is high, thus obstructing the hard photons coming from the inner and hotter region of the accretion disk (see similar discussion for NGC 55 ULX in Pinto et al. (2017)).

The power spectrum analysis of the time series shows low frequency red noise explained by power-law type PSD in a few observations. This often occurs in X-ray binaries due to variation in mass accretion rate (Uttley & McHardy 2001). We do not find any quasi-periodic or periodic oscillation on top of the red and white noise in the power spectrum. The soft and hard energy time series in XM2 and XM4 epochs confirm that the harder spectral components dominate the flaring activity. A comparable behavior in other ULXs (e.g. Gúrpidé et al. 2021a,b) can be interpreted as the partial occultation of the inner region of the disk from the wind launched by the super-Eddington disk. This might in principle be the explanation for our results, but we caution that our source has a much lower luminosity than the soft-

ultraluminous ULXs showing that behavior. Another possibility is that we are witnessing a genuine change of accretion rate, leading to the flaring behavior. An advection-dominated disk, in the absence of beaming, is expected to show a $L \propto T^2$ relation. This might very well be the case in our data, as shown in figure 4, where we plot the unabsorbed DISKPBB component luminosity (0.3–10.0 keV) and the corresponding disk temperature.

The accretion rate of a slim disk in the presence of advection relates to the luminosity as $L \sim L_{edd}[1 + \ln \dot{m}]$, where \dot{m} is the Eddington factor, ratio of the accretion rate to the Eddington accretion rate (Shakura & Sunyaev 1973). The ratio of the luminosity during flares to the non-flare periods ($\frac{L_{flare}}{L_{non-flare}} \sim 2$) can then be used to estimate the change of mass accretion rate. Simple algebra leads to the relation of corresponding Eddington factors of $\dot{m}_{flare} \simeq e \cdot \dot{m}_{non-flare}^2$.

Some authors propose that an apparent change of luminosity in super-Eddington disks might be dominated by the geometrical beaming from the disk winds. In this case, $L \propto L_{edd}[1 + \ln \dot{m}] \dot{m}^2$, because beaming is proportional to $73/\dot{m}^2$ (King 2009; King & Lasota 2016; King et al. 2017). Since the luminosity ratio in this case is small (~ 2), the luminosity-accretion rate relation can be approximated to $\frac{L_{flare}}{L_{non-flare}} \sim \frac{\dot{m}_{flare}^2}{\dot{m}_{non-flare}^2}$. In that scenario, the Eddington factors corresponding to

flaring and non-flaring episodes follow a simple form of $\dot{m}_{flare} \simeq \sqrt{2}\dot{m}_{non-flare}$.

The accretion disk normalizations provide an estimate for the inner radius $R_{in} \simeq \xi \kappa^2 N^{\frac{1}{2}} d_{10} (\cos \theta)^{-\frac{1}{2}}$ km, where ξ is the geometric correction factor and κ is the color correction factor, d_{10} is the distance in 10 kpc unit, N is the normalization and θ is the inclination angle of the disk (Soria et al. 2015; Walton et al. 2020; Ghosh & Rana 2021). We estimate the inner radius from the disk normalizations for all the four epochs XM1, XM2, XM3 and XM4. We understand that due to large uncertainty in the DISKBB normalization measurement in different epochs, the thin accretion disk radius can have a large range of values between $\sim 2000(\cos \theta)^{-\frac{1}{2}}$ km to $\sim 7000(\cos \theta)^{-\frac{1}{2}}$ km assuming $\xi \sim 0.412$ and $\kappa \sim 1.7$ (Soria et al. 2015). The DISKPBBS slim accretion disk normalizations are however similar in different epochs, hence the inner radius is found by taking an average DISKPBBS normalization of all the four epochs XM1, XM2, XM3 and XM4. Under the assumption of $\xi \sim 0.353$ and $\kappa \sim 3$ for a slim disk (Soria et al. 2015), the radius turns out to be $273^{+98}_{-166}(\cos \theta)^{-\frac{1}{2}}$ km. This would correspond to the last stable orbit ($R_{ISCO} = 6GM/c^2$) of a $\sim 30 M_{\odot}$ non-rotating black hole assuming a face on disk, or to the magnetospheric radius ($R_M = 7 \times 10^7 \Lambda m^{\frac{1}{2}} R_6^{\frac{10}{3}} B_{12}^{\frac{4}{3}} L_{39}^{-\frac{2}{3}}$ cm; parameters are explained in Mushtukov et al. (2017)) of a magnetized neutron star of $1.4 M_{\odot}$ with a magnetic field of $\sim 8.6 \times 10^{11}$ Gauss. We have used the typical values of $\Lambda \sim 0.5$, $R_6 \sim 10^6$ cm, and L_{39} is the average luminosity measured for the four epochs $\sim 2.1 \times 10^{39} \text{ erg s}^{-1}$.

Some of the harder photons in ULX1 may also be generated from the inverse-Compton scattering process in the Coronal region near the inner disk. The flaring events can have a much more significant up-scattered photon fraction due to proliferation in numbers of inner disk photons. However, quantifying Compton scattering process require high energy data coverage (Ghosh & Rana 2021; Walton et al. 2020) which is not available for NGC 4395 ULX1. Future observations with hard X-ray instruments like *NuSTAR* may uncover the Comptonization scenario with much better constraints.

If this interpretation is true, it is the inner disk component that is dominating the variable part of the spectrum. This might be due either to an intrinsic change of accretion rate, or to a variable clumpy wind that partially occultates the inner region and imprints this variability on the hard emission. However, the absorp-

tion column density remains unchanged in these observations. This suggests that such transient flaring phenomena are related to the inner disk region far distanced from the wind cloud regions where the emission line generates.

NGC 4395 ULX1 showed a clear broad emission feature around 0.9 keV. Similar feature has been reported in several other ULXs like NGC 1313 X1, NGC 55 ULX, NGC 247 ULX-1 (Pinto et al. 2017, 2020, 2021). This broad ~ 0.9 keV line feature is in reality a combination of multiple emission lines which cannot be resolved by EPIC instruments. These lines are typically blue-shifted Mg XII, Fe XXII-XXIII, Ne X, Ne IX, O VIII, and O VII lines. The signal-to-noise ratio in RGS data is poor for ULX1 in all four observations, and the background mostly dominates the whole RGS spectra. Hence, we could not use RGS data to quantify any emission or absorption feature present in the source. While our time-resolved spectroscopy suggests that the spectra become harder with transient flaring events, the wind outflow, which is a direct measure of the emission lines, is not significantly affected by these transient events. At least, within the limitation of current data, we cannot find any deviation in the overall line strength in different epochs. In fact, below ~ 1 keV, spectral and timing properties of flaring epochs remain the same as of non-flaring epochs.

Future detection of this source in difference flux states with broadband X-ray coverage can put better constraints on physical parameters we establish in this paper.

The scientific results reported in this article have used archival data (available at the High Energy Astrophysics Science Archive Research Center (HEASARC)) obtained with *XMM-NEWTON*, an ESA science mission with instruments and contributions directly funded by ESA member states and NASA.

Facilities: XMM-NEWTON

Software: HEASOFT (<https://heasarc.gsfc.nasa.gov/docs/software/heasoft/>), *XMM-NEWTON SAS* (<https://www.cosmos.esa.int/web/xmm-newton/sas>), HENDRICS (<https://hendrics.stingray.science/en/latest/>), PRESTO (<https://github.com/scottransom/presto>)

REFERENCES

- Bachetti, M. 2018, HENDRICS: High ENergy Data Reduction Interface from the Command Shell. <http://ascl.net/1805.019>
- Bachetti, M., Harrison, F. A., Walton, D. J., et al. 2014, *Nature*, 514, 202, doi: [10.1038/nature13791](https://doi.org/10.1038/nature13791)

- Barnard, R. 2010, MNRAS, 404, 42, doi: [10.1111/j.1365-2966.2010.16291.x](https://doi.org/10.1111/j.1365-2966.2010.16291.x)
- Brightman, M., Harrison, F. A., Barret, D., et al. 2016, The Astrophysical Journal, 829, 28, doi: [10.3847/0004-637x/829/1/28](https://doi.org/10.3847/0004-637x/829/1/28)
- Brightman, M., Harrison, F. A., Fürst, F., et al. 2018, Nature Astronomy, 2, 312, doi: [10.1038/s41550-018-0391-6](https://doi.org/10.1038/s41550-018-0391-6)
- Carpino, S., Haberl, F., Maitra, C., & Vasilopoulos, G. 2018, MNRAS, 476, L45, doi: [10.1093/mnrasl/sly030](https://doi.org/10.1093/mnrasl/sly030)
- Chandra, A. D., Roy, J., Agrawal, P. C., & Choudhury, M. 2020, MNRAS, 495, 2664, doi: [10.1093/mnras/staa1041](https://doi.org/10.1093/mnras/staa1041)
- Earnshaw, H. M., & Roberts, T. P. 2017, MNRAS, 467, 2690, doi: [10.1093/mnras/stx308](https://doi.org/10.1093/mnras/stx308)
- Earnshaw, H. P., Grefenstette, B. W., Brightman, M., et al. 2019, ApJ, 881, 38, doi: [10.3847/1538-4357/ab20cd](https://doi.org/10.3847/1538-4357/ab20cd)
- Edelson, R., Turner, T. J., Pounds, K., et al. 2002, ApJ, 568, 610, doi: [10.1086/323779](https://doi.org/10.1086/323779)
- Fürst, F., Walton, D. J., Harrison, F. A., et al. 2016, ApJL, 831, L14, doi: [10.3847/2041-8205/831/2/L14](https://doi.org/10.3847/2041-8205/831/2/L14)
- Ghosh, T., & Rana, V. 2021, MNRAS, 504, 974, doi: [10.1093/mnras/stab774](https://doi.org/10.1093/mnras/stab774)
- Gürpide, A., Godet, O., Koliopanos, F., Webb, N., & Olive, J. F. 2021a, A&A, 649, A104, doi: [10.1051/0004-6361/202039572](https://doi.org/10.1051/0004-6361/202039572)
- Gürpide, A., Godet, O., Vasilopoulos, G., Webb, N. A., & Olive, J. F. 2021b, A&A, 654, A10, doi: [10.1051/0004-6361/202140781](https://doi.org/10.1051/0004-6361/202140781)
- Israel, G. L., Belfiore, A., Stella, L., et al. 2017a, Science, 355, 817, doi: [10.1126/science.aai8635](https://doi.org/10.1126/science.aai8635)
- Israel, G. L., Papitto, A., Esposito, P., et al. 2017b, MNRAS, 466, L48, doi: [10.1093/mnrasl/slw218](https://doi.org/10.1093/mnrasl/slw218)
- Kaaret, P., & Feng, H. 2009, ApJ, 702, 1679, doi: [10.1088/0004-637X/702/2/1679](https://doi.org/10.1088/0004-637X/702/2/1679)
- Kaaret, P., Feng, H., & Roberts, T. P. 2017, ARA&A, 55, 303, doi: [10.1146/annurev-astro-091916-055259](https://doi.org/10.1146/annurev-astro-091916-055259)
- Kara, E., Pinto, C., Walton, D. J., et al. 2020, MNRAS, 491, 5172, doi: [10.1093/mnras/stz3318](https://doi.org/10.1093/mnras/stz3318)
- King, A., & Lasota, J.-P. 2016, MNRAS, 458, L10, doi: [10.1093/mnrasl/slw011](https://doi.org/10.1093/mnrasl/slw011)
- King, A., Lasota, J.-P., & Kluźniak, W. 2017, MNRAS, 468, L59, doi: [10.1093/mnrasl/slx020](https://doi.org/10.1093/mnrasl/slx020)
- King, A. R. 2009, MNRAS, 393, L41, doi: [10.1111/j.1745-3933.2008.00594.x](https://doi.org/10.1111/j.1745-3933.2008.00594.x)
- Kosec, P., Pinto, C., Fabian, A. C., & Walton, D. J. 2018a, MNRAS, 473, 5680, doi: [10.1093/mnras/stx2695](https://doi.org/10.1093/mnras/stx2695)
- Kosec, P., Pinto, C., Walton, D. J., et al. 2018b, MNRAS, 479, 3978, doi: [10.1093/mnras/sty1626](https://doi.org/10.1093/mnras/sty1626)
- Liu, J.-F., & Bregman, J. N. 2005, ApJS, 157, 59, doi: [10.1086/427170](https://doi.org/10.1086/427170)
- Middleton, M. J., Walton, D. J., Fabian, A., et al. 2015, MNRAS, 454, 3134, doi: [10.1093/mnras/stv2214](https://doi.org/10.1093/mnras/stv2214)
- Motta, S. E., Marelli, M., Pintore, F., et al. 2020, ApJ, 898, 174, doi: [10.3847/1538-4357/ab9b81](https://doi.org/10.3847/1538-4357/ab9b81)
- Mushtukov, A. A., Suleimanov, V. F., Tsygankov, S. S., & Ingram, A. 2017, MNRAS, 467, 1202, doi: [10.1093/mnras/stx141](https://doi.org/10.1093/mnras/stx141)
- Pinto, C., Middleton, M. J., & Fabian, A. C. 2016, Nature, 533, 64, doi: [10.1038/nature17417](https://doi.org/10.1038/nature17417)
- Pinto, C., Alston, W., Soria, R., et al. 2017, MNRAS, 468, 2865, doi: [10.1093/mnras/stx641](https://doi.org/10.1093/mnras/stx641)
- Pinto, C., Walton, D. J., Kara, E., et al. 2020, MNRAS, 492, 4646, doi: [10.1093/mnras/staa118](https://doi.org/10.1093/mnras/staa118)
- Pinto, C., Soria, R., Walton, D., et al. 2021, arXiv e-prints, arXiv:2104.11164. <https://arxiv.org/abs/2104.11164>
- Pintore, F., Marelli, M., Salvaterra, R., et al. 2020, ApJ, 890, 166, doi: [10.3847/1538-4357/ab6ffd](https://doi.org/10.3847/1538-4357/ab6ffd)
- Pintore, F., Motta, S., Pinto, C., et al. 2021, MNRAS, 504, 551, doi: [10.1093/mnras/stab913](https://doi.org/10.1093/mnras/stab913)
- Poutanen, J., Lipunova, G., Fabrika, S., Butkevich, A. G., & Abolmasov, P. 2007, MNRAS, 377, 1187, doi: [10.1111/j.1365-2966.2007.11668.x](https://doi.org/10.1111/j.1365-2966.2007.11668.x)
- Ransom, S. 2011, PRESTO: Pulsar Exploration and Search TOokit. <http://ascl.net/1107.017>
- Rodríguez Castillo, G. A., Israel, G. L., Belfiore, A., et al. 2020, ApJ, 895, 60, doi: [10.3847/1538-4357/ab8a44](https://doi.org/10.3847/1538-4357/ab8a44)
- Sathyaprakash, R., Roberts, T. P., Walton, D. J., et al. 2019, MNRAS, 488, L35, doi: [10.1093/mnrasl/slz086](https://doi.org/10.1093/mnrasl/slz086)
- Shakura, N. I., & Sunyaev, R. A. 1973, A&A, 500, 33
- Soria, R., Kuntz, K. D., Long, K. S., et al. 2015, ApJ, 799, 140, doi: [10.1088/0004-637X/799/2/140](https://doi.org/10.1088/0004-637X/799/2/140)
- Sutton, A. D., Roberts, T. P., & Middleton, M. J. 2013, MNRAS, 435, 1758, doi: [10.1093/mnras/stt1419](https://doi.org/10.1093/mnras/stt1419)
- Uttley, P., & McHardy, I. M. 2001, MNRAS, 323, L26, doi: [10.1046/j.1365-8711.2001.04496.x](https://doi.org/10.1046/j.1365-8711.2001.04496.x)
- Vaughan, S., Edelson, R., Warwick, R. S., & Uttley, P. 2003, MNRAS, 345, 1271, doi: [10.1046/j.1365-2966.2003.07042.x](https://doi.org/10.1046/j.1365-2966.2003.07042.x)
- Verner, D. A., Ferland, G. J., Korista, K. T., & Yakovlev, D. G. 1996, ApJ, 465, 487, doi: [10.1086/177435](https://doi.org/10.1086/177435)
- Vinokurov, A., Fabrika, S., & Atapin, K. 2018, ApJ, 854, 176, doi: [10.3847/1538-4357/aaaa6c](https://doi.org/10.3847/1538-4357/aaaa6c)
- Walton, D. J., Middleton, M. J., Pinto, C., et al. 2016, ApJL, 826, L26, doi: [10.3847/2041-8205/826/2/L26](https://doi.org/10.3847/2041-8205/826/2/L26)
- Walton, D. J., Pinto, C., Nowak, M., et al. 2020, MNRAS, 494, 6012, doi: [10.1093/mnras/staa1129](https://doi.org/10.1093/mnras/staa1129)
- Wilms, J., Allen, A., & McCray, R. 2000, ApJ, 542, 914, doi: [10.1086/317016](https://doi.org/10.1086/317016)